Glacial reduction and millennial-scale variations in Drake Passage throughflow

Frank Lamy[a,1], Helge W. Arz[b], Rolf Kilian[c,d], Carina B. Lange[e], Lester Lembke-Jene[a], Marc Wengler[a], Jérôme Kaiser[b], Oscar Baeza-Urrea[c], Ian R. Hall[f], Naomi Harada[g], and Ralf Tiedemann[a]

[a]Marine Geology Section, Alfred-Wegener-Institut Helmholtz-Zentrum für Polar- und Meeresforschung, 27570 Bremerhaven, Germany; [b]Department of Marine Geology, Leibniz Institute for Baltic Sea Research, 18119 Rostock-Warnemünde, Germany; [c]Geologie, Fachbereich Raum- und Umweltwissenschaften, Universität Trier, 54286 Trier, Germany; [d]Instituto de la Patagonia, Universidad de Magallanes, 6200000 Punta Arenas, Chile; [e]Department of Oceanography and Center for Oceanographic Research in the Eastern South Pacific (COPAS), COPAS Sur-Austral Program, University of Concepción, 4030000 Concepción, Chile; [f]School of Earth and Ocean Sciences, Cardiff University, Cardiff CF10 3AT, United Kingdom; and [g]Research and Development Center for Global Change, Japan Agency for Marine-Earth Science and Technology, Yokosuka 237-0061, Japan

Edited by Mark H. Thiemens, University of California at San Diego, La Jolla, CA, and approved July 31, 2015 (received for review May 12, 2015)

The Drake Passage (DP) is the major geographic constriction for the Antarctic Circumpolar Current (ACC) and exerts a strong control on the exchange of physical, chemical, and biological properties between the Atlantic, Pacific, and Indian Ocean basins. Resolving changes in the flow of circumpolar water masses through this gateway is, therefore, crucial for advancing our understanding of the Southern Ocean's role in global ocean and climate variability. Here, we reconstruct changes in DP throughflow dynamics over the past 65,000 y based on grain size and geochemical properties of sediment records from the southernmost continental margin of South America. Combined with published sediment records from the Scotia Sea, we argue for a considerable total reduction of DP transport and reveal an up to ∼40% decrease in flow speed along the northernmost ACC pathway entering the DP during glacial times. Superimposed on this long-term decrease are high-amplitude, millennial-scale variations, which parallel Southern Ocean and Antarctic temperature patterns. The glacial intervals of strong weakening of the ACC entering the DP imply an enhanced export of northern ACC surface and intermediate waters into the South Pacific Gyre and reduced Pacific–Atlantic exchange through the DP ("cold water route"). We conclude that changes in DP throughflow play a critical role for the global meridional overturning circulation and interbasin exchange in the Southern Ocean, most likely regulated by variations in the westerly wind field and changes in Antarctic sea ice extent.

paleoceanography | Drake Passage | Antarctic Circumpolar Current | glacial–interglacial changes | sedimentology

The Antarctic Circumpolar Current (ACC) is the world's largest current system. Through inducing pronounced upwelling and formation of new water masses, the ACC fundamentally affects the global meridional overturning circulation (1) and the stability of Antarctica's ice sheets. The flow of the ACC is largely driven by strong westerly winds and constricted to its narrowest extent in the Drake Passage (DP). This so-called "cold water route" transport through the DP is one important pathway for the return of fresh and cold waters to the Atlantic, which strongly affects the strength of the Atlantic meridional overturning circulation, in concert with the "warm water route" inflow of warm and salty Indian Ocean water masses through the Agulhas Current system (2, 3).

The DP is ∼800-km wide and located between Cape Horn and the western Antarctic Peninsula (Fig. 1). Numerous hydrographic surveys across the DP since the 1970s have contributed to the understanding of yearlong and interannual variability in ACC transport through the DP and the mechanisms forcing physical and biological changes within the Southern Ocean (4, 5). However, even with hydrographic time series reaching back 20 y (6) in this well-constrained region of the ACC and more sophisticated model simulations (7), important issues such as the role of zonal winds in forcing ACC transport remain controversial.

Compared with other parts of the Southern Ocean, the modern oceanography of the ACC within the DP is well-monitored. The three major ACC oceanographic fronts (8) [the sub-Antarctic Front (SAF), the Polar Front (PF), and the Southern ACC Front (SACCF)] can be identified from north to south within the DP. The exact location and occurrence of subsidiary fronts change from year to year and strongly affect the current velocity pattern across the DP (6, 9, 10) (Fig. 2*B*). The modern winter sea ice margin presently does not extend significantly north into the DP (11). The total ACC volume transported through the DP is estimated between ∼130 and 150 Sv (4–6, 9). The many oceanographic studies robustly show that more than one-half of the total DP transport occurs at and north of the SAF (i.e., in the sub-Antarctic Zone) followed by the Polar Frontal Zone (between the SAF and the PF) (Fig. 2*A*). The relative contribution of DP transport south of the PF is generally less than 20%.

Available proxy data and model simulations provide only little information on the potential role of the DP region in driving changes in the global ocean circulation at glacial–interglacial and millennial timescales (12, 13). Downstream of the DP, a meridional section of low-resolution records from the Scotia Sea revealed little overall bottom current speed variations between the Last Glacial Maximum (LGM) sensu lato (18–28 ka) and the Holocene (13). In contrast, a 500,000-y record from the southern Indian Ocean (eastward from the Crozet–Kerguelen Plateau) suggests that the ACC was weak during warm stages and strong

Significance

The Drake Passage (DP) represents the most important oceanic gateway along the pathway of the world's largest current: the Antarctic Circumpolar Current (ACC). Resolving changes in the flow of circumpolar water masses through the DP is crucial for advancing our understanding of the Southern Ocean's role in affecting ocean and climate change on a global scale. We reconstruct current intensity from marine sediment records around the southern tip of South America with unprecedented millennial-scale resolution covering the past ∼65,000 y. For the last glacial period, we infer intervals of strong weakening of the ACC entering the DP, implying an enhanced export of northern ACC surface and intermediate waters into the South Pacific Gyre and reduced Pacific–Atlantic exchange through the cold water route.

Author contributions: F.L., H.W.A., C.B.L., J.K., and R.T. designed research; M.W., O.B.-U., I.R.H., and N.H. contributed analytic tools; F.L., H.W.A., R.K., and N.H. analyzed data; and F.L., C.B.L., L.L.-J., J.K., I.R.H., and R.T. wrote the paper.

The authors declare no conflict of interest.

This article is a PNAS Direct Submission.

Freely available online through the PNAS open access option.

Data deposition: The data reported in this paper are available at doi.pangaea.de/10.1594/PANGAEA.848152.

[1]To whom correspondence should be addressed. Email: Frank.Lamy@awi.de.

This article contains supporting information online at www.pnas.org/lookup/suppl/doi:10.1073/pnas.1509203112/-/DCSupplemental.

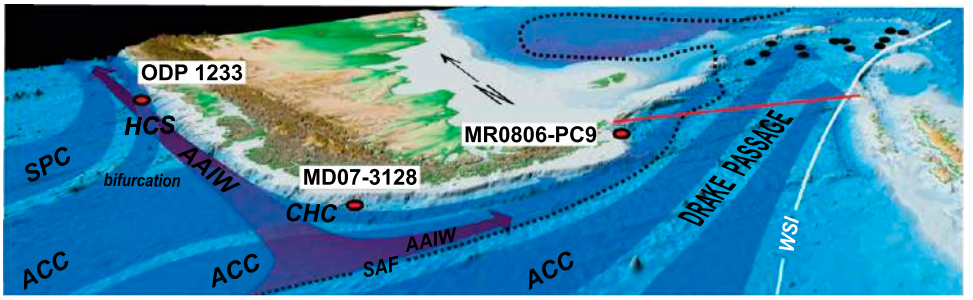

Fig. 1. Schematic view of the DP region with major surface and intermediate water circulation and location of the sediment cores discussed (labeled red dots refer to our data, and unlabeled black dots indicate locations of cores in the Scotia Sea) (13). The red line across the DP shows the oceanographic Jason Track 104 (6). Approximate locations are based on the works by Orsi et al. (8) and Comiso et al. (11). AAIW, Antarctic Intermediate Water; HCS, Humboldt Current System; SPC, South Pacific Current; WSI, winter sea ice.

during glacial epochs (14). Likewise, in the Southwest Pacific, the deep western boundary current east of New Zealand intensified during glacial periods over the past 1.2 My (15), which has been related to a northward extension of the ACC along the New Zealand continental margin (15, 16). Evidently, disagreement exists for ACC flow intensity and its potential impact on changes in DP throughflow in response to glacial and interglacial cycles.

Results and Discussion

Because of strong bottom currents and severe weather conditions, the recovery of sediment records directly within the DP is difficult. We, therefore, address changes in northern DP throughflow with high-resolution sediment records recovered from the southernmost Chilean continental slope directly upstream of the DP (core MD07-3128; 52°39.57′ S, 75°33.97′ W; 1,032-m water depth) and the Argentinian continental slope east of Cape Horn at the northern margin of the DP (core MR0806-PC09; 55°42.58′ S, 66°08.06′ W; 684-m water depth) (Fig. 1). Core MD07-3128 is located underneath the southward flowing Cape Horn Current (CHC), a northern branch of the ACC that continues toward the DP and provides a major fraction of the present day northern DP transport (17). Satellite-tracked surface drifters reveal that, after crossing the East Pacific Rise, sub-Antarctic Surface Water of the ACC is transported northeastward across the Southeast Pacific toward the Chilean coast at ∼45° S/75° W (18) (Fig. 1 and Fig. S1). Here, presently only a minor part of ACC water is deflected northward into the Humboldt Current System, whereas the major fraction is deviated southward toward the DP. The CHC, thus, transports a significant amount of northern ACC water toward the DP within a narrow belt of ∼100–150-km width off the coast (18) (Fig. S1).

Site MD07-3128 provides an ∼30-m-long sediment core spanning the past ∼65,000 y (*SI Methods* and Table S1). The age model [updated from the work by Caniupán et al. (19)] is well-constrained by radiocarbon dating, the occurrence of the Laschamp paleomagnetic excursion, and correlation to the well-dated sediment record from Ocean Drilling Program Site 1233 (20). High sedimentation rates during most of the glacial section (Fig. S2) allow the investigation of CHC strength changes at millennial timescales as an approximation of the northern ACC fraction of DP throughflow. Previous work on this core revealed substantial fluctuations of sea surface temperatures (SSTs) that largely follow the timing of temperature fluctuations observed in Antarctic ice cores (19). The lower-resolved, radiocarbon-dated core MR0806-PC09 [age model updated from the work by Shiroya et al. (21)] is used to complement glacial–interglacial ACC strength estimates directly within the northern sector of the DP.

Sedimentological and Geochemical Current Strength Proxies. To reconstruct variations in the CHC/northern ACC flow speed, we use changes in grain size and geochemical properties (*SI Methods*). Our current strength proxies are the weight percentages of the 63- to 150-μm fine-sand fraction and the mean sortable silt (SS) grain size ($\overline{SS}$; 10–63 μm) of the terrigenous sediment fraction (Figs. S3 and S4). The $\overline{SS}$ proxy is commonly used for estimating relative changes in the near-bottom flow speed in deep sea sediments (22). Modern surface current velocities within the CHC of >35 cm/s (18) and high flow speeds of ∼20 cm/s extending to middepths (Fig. S1), as suggested by vertical current speed profiles in the CHC (23) and the DP (24), reasonably explain the coarse-grain size

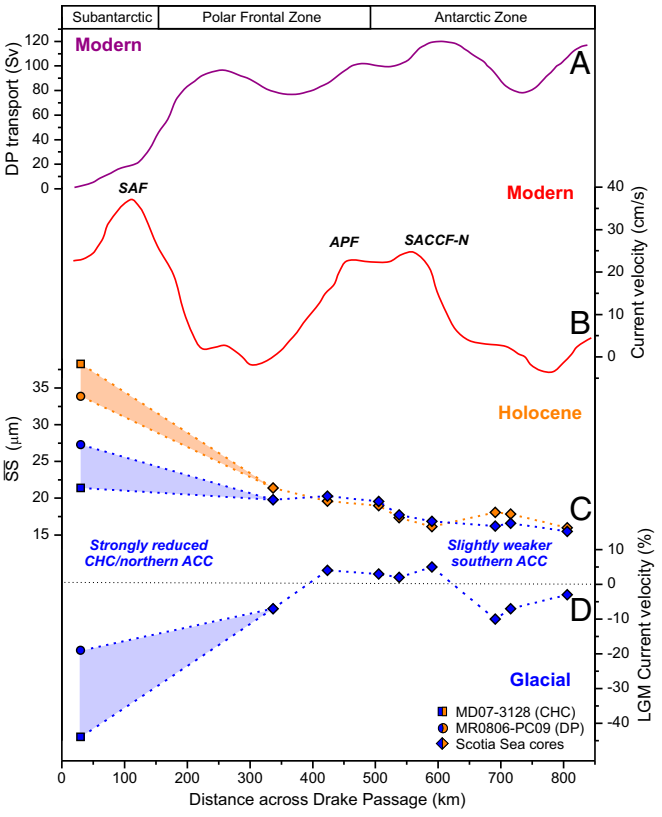

Fig. 2. DP throughflow during the LGM compared with the modern setting. (*A*) Modern DP cumulative volume transport above 3,000-m water depth. Values are cumulated along DP Jason Track 104 (Fig. 1 and Fig. S1) from north to south. (*B*) The volume transport is calculated from across-track surface geostrophic velocities (6). Front positions based on the geostrophic velocities. (*C*) Holocene and glacial (LGM sensu lato, 18–28 ka) mean $\overline{SS}$ data across the DP, including data south of the SAF in the Scotia Sea (13). Note that the Holocene pattern reflects the northward increase in ACC flow across the DP. The location of each core was projected on the oceanographic Jason Track 104 (*SI Methods*). Error estimates ($2\sigma/\sqrt{n}$) are shown in Table S2. (*D*) Current speed changes (percentages) during the LGM sensu lato. Compared with the Holocene, mean LGM values are lower by ∼40% below the CHC and ∼20% in the northern DP, suggesting a substantial reduction of the sub-Antarctic ACC contribution to DP throughflow. APF, Antarctic Polar; SACCF-N, northern branch of the southern ACC front.

distributions observed during the Holocene (Figs. S3 and S4). $\overline{SS}$ data have been regionally calibrated with instrumental current meter data showing a linear relationship (25, 26). The inference of flow intensity may be complicated by changes in sediment supply. Indeed, previous work at site MD07-3128 has shown that glacial sediments contain ice-rafted debris (>150 μm) (19). Additional changes in sediment supply might be expected as the modern sediment depocenters in the proximal fjord systems become inactive with lower sea level during glacials. However, the deposition of ice-rafted debris at site MD07-3128 shows fluctuations that are independent of $\overline{SS}$ and fine-sand contents (Fig. S3). Moreover, changes in $\overline{SS}$ and the weight percentage of the SS component are positively correlated, which is a strong argument for primarily current-controlled grain size changes within the silt fraction (13) (Fig. S3).

Substantial changes in the geochemical composition of the sediments parallel grain size fluctuations at the CHC site MD07-3128 (Fig. S5). The different grain size and geochemical indicators show excellent correlations. Most notably, higher Zr/Rb and Si/Al ratios occur in the coarser-grained intervals as typical indicators for sediments affected by changes in current strength or eolian input (27). Because biogenic opal contents are minor (1–4 wt %), we interpret high Zr and Si contents to reflect coarser siliciclastic sediment components, whereas finer-grained minerals, including clay minerals, are more Rb- and Al-rich. Thus, ample changes in CHC strength and underlying water masses are revealed by the large grain size and sediment composition changes.

Evidence for a Glacial Reduction of DP Transport. At site MD07-3128 below the CHC, the Holocene average SS grain size is ~38 μm (Table S1). Using the latest calibration of $\overline{SS}$ with North Atlantic current meter data (26), these $\overline{SS}$ values translate to current speeds of ~36 cm/s, consistent with modern velocity estimates within the CHC (18). During the LGM, the average $\overline{SS}$ is ~21 μm, indicating that the CHC strength was reduced by ~40% (Fig. 2 *C* and *D*). This strong decrease of flow speeds in the CHC implies a weakening of the northern (sub-Antarctic) ACC limb entering the DP. This paleoceanographic inference is strongly supported by the geographic pattern of SST cooling in the South Pacific during the LGM (Fig. 3 and Table S3). In the eastern sub-Antarctic Pacific, the pronounced cooling of up to ~7 °C is considerably larger than in the central sub-Antarctic Pacific and implies a strong northward extension of the Antarctic cold water influence in the Southeast Pacific during glacial conditions (28). The cold water expansion decreases the backflow of northern ACC water through the CHC to the DP but enhances its export into the South Pacific Gyre as indicated by the strong cooling observed in published SST records along the Humboldt Current system (Fig. 3 and Table S3). A similar northward extension of cold ACC waters occurred in the Southwest Pacific off New Zealand (16, 29).

The reduction of northern (sub-Antarctic) ACC flow as reconstructed from our CHC core MD07-3128 is also evident at our northern DP margin record (MR0806-PC09), which reveals ~20% finer $\overline{SS}$ values (Fig. 2 *C* and *D*). The lower amplitude of the

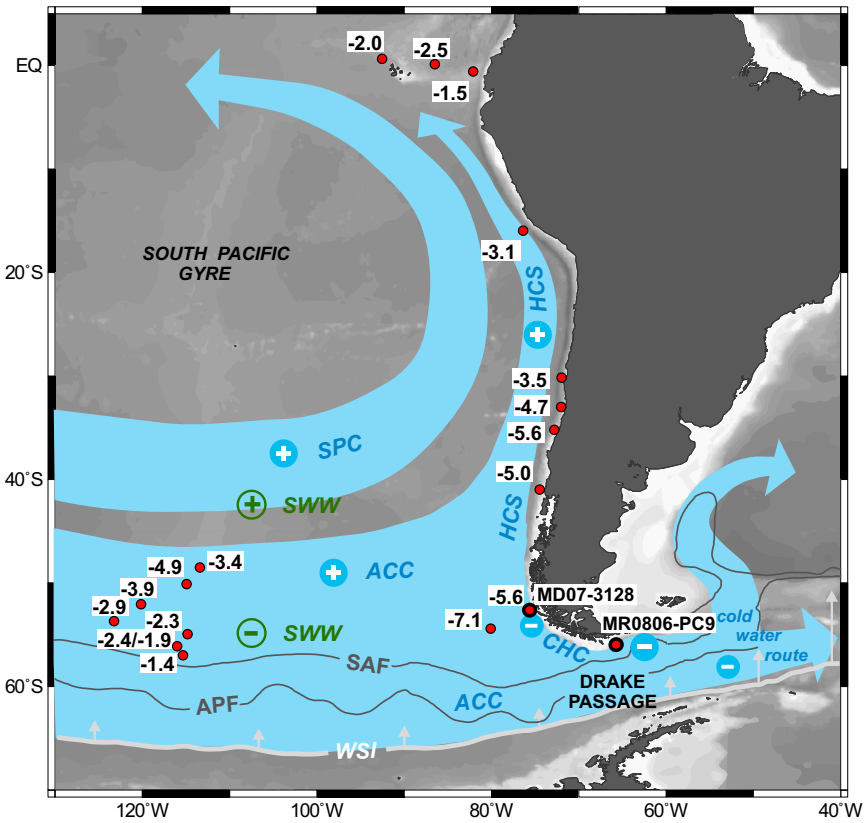

Fig. 3. Map showing LGM paleoceanography of the Southeast Pacific and DP region. The pronounced glacial cooling in the eastern sub-Antarctic Pacific is consistent with a northward extension of Antarctic cold water influence [numbers indicate LGM cooling (degrees Celsius) compared with the Holocene mean, and red dots show locations of SST sediment records] (*Methods* and Table S3). Reduced CHC and more sluggish glacial northern DP transport decrease the export of Pacific ACC water into the South Atlantic (cold water route). Reduced SWW core and extended sea ice diminish the wind forcing on the ACC and thus, the DP transport. Stronger winds in the northern SWW enhance the South Pacific Gyre and the export of northern ACC water into the Humboldt Current System (HCS). Background shows bathymetry. Modern locations are based on the works by Orsi et al. (8) and Comiso et al. (11). APF, Antarctic PF; SPC, South Pacific Current; WSI, winter sea ice.

glacial–interglacial $\overline{SS}$ change at this site might indicate an amplification of the signal within the CHC (for example, through variations in the vertical structure of the flow along the South American continental margin). However, the few available vertical current strength profiles from the CHC show that the high velocities reach down to >2,000-m water depth (23), and we, therefore, do not expect large modifications of the vertical flow structure at our site since the last glacial. Alternatively, the northern DP record from core MR0806-PC09 might underestimate the glacial flow decrease because of the rather complex flow geometry with major eddy structures in this region (6, 9, 30). Taken together, qualitatively, our two sediment core records uniformly document a substantial decrease in sub-Antarctic CHC/northern ACC flow speeds upstream and within the DP.

A more reliable quantification of the glacial flow speed decrease in the sub-Antarctic section of the DP would require a more densely spaced core transect in the future. To obtain a more comprehensive view of last glacial changes in ACC flow in the vicinity of the DP, we combined our sub-Antarctic ACC flow speed estimates upstream and within the DP with the published data from the central Scotia Sea downstream of the DP (13) (Figs. 1 and 2 and Table S2). Together, these records extend across all major modern oceanographic zones within the ACC and DP. During the LGM, the combined $\overline{SS}$ data indicate a strong reduction in flow speed in the northern sector (modern sub-Antarctic Zone) that extends to the present Polar Frontal Zone, whereas only minor changes occur south of the PF, except for a slight reduction in glacial ACC flow in the southern Antarctic Zone (Fig. 2). Modern oceanography suggests that current velocities and transport are overall closely linked in the DP region, with the major transport and the highest current velocities occurring in the sub-Antarctic Zone (Fig. 2*B*) (5, 6, 9). Therefore, we interpret our paleodata in terms of a substantial LGM decrease of sub-Antarctic DP throughflow combined with an additional slight reduction of ACC transport in the glacially extended sea ice zone (13).

Today, Antarctic Intermediate Water (AAIW) formed in the Southeast Pacific is partly exported into the South Atlantic (31). Strongly reduced CHC vigor and more sluggish DP transport during the LGM would plausibly decrease the export of Pacific surface and intermediate water masses into the South Atlantic and thus, reduce the cold water route contribution. Such glacial Southern Ocean circulation is in accordance with a stronger South Pacific Gyre and the export of well-oxygenated AAIW along the Chilean margin (32, 33). Concurrently, proxy data indicate poorly ventilated intermediate waters in the glacial South Atlantic as contributions from the Pacific and Indian Oceans were reduced (34), consistent with reduced export from the major modern intermediate water formation region in the Southeast Pacific through the DP (Fig. 1). Our suggested strongly enhanced glacial northward export of cold water masses to the tropical Pacific (Fig. 3) reinforces earlier modeling studies showing the importance of southerly derived surface and intermediate water masses in the tropical Pacific for global cooling during the LGM (35).

Millennial-Scale Variations During the Last Glacial. Superimposed on the long-term glacial reduction of DP throughflow, we observe prominent high-amplitude, millennial-scale variability in the CHC/northern ACC flow speeds (Fig. 4), which is not resolved in the Scotia Sea records or any other previous ACC current strength record (13, 14). Substantial changes in the geochemical sediment composition parallel these grain size fluctuations (Fig. S5). Within age model uncertainties, most of the grain size maxima coincide with millennial-scale temperature maxima in Antarctica (36) (Fig. 4), implying a strong sensitivity of the CHC and the northern ACC in the Southeast Pacific to suborbital climate variations. This pattern is particularly evident for the major Antarctic warmings

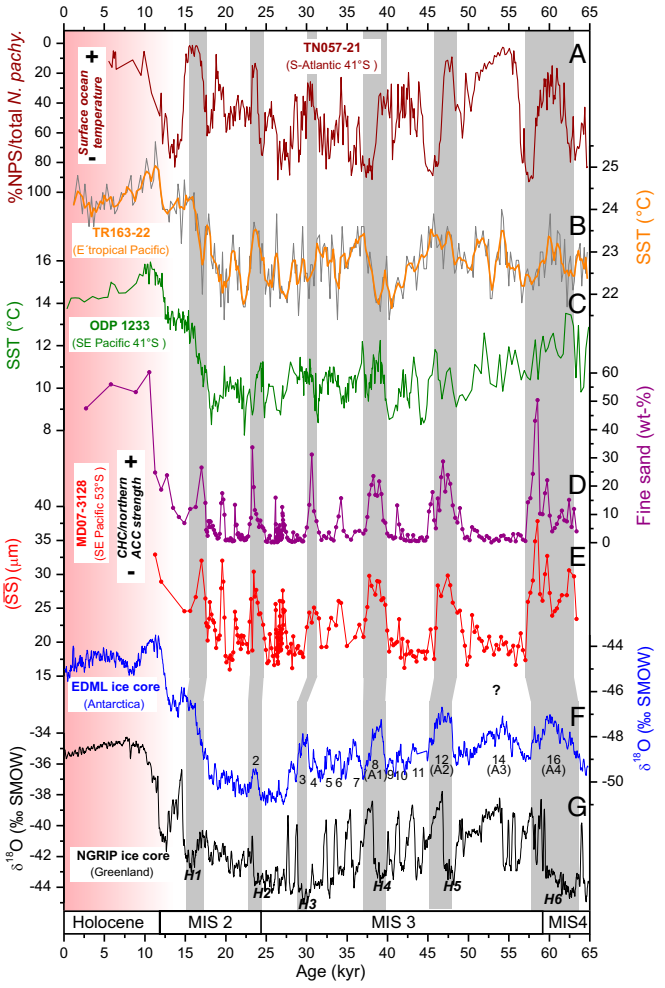

Fig. 4. Reconstructed changes in CHC strength and DP throughflow compared with temperature records. (*A*) Ratio of planktic foraminifera *Neogloboquadrina pachyderma* (NPS) to total NPS counts indicative of surface ocean temperature changes in the South Atlantic (42). (*B*) Mg/Ca SST record from the Galapagos region (43) representing eastern tropical Pacific SST changes. (*C*) Alkenone SST record from Ocean Drilling Program (ODP) Site 1233 located within the Humboldt Current System (HCS) at ~41° S (20) (updated age model) (*SI Methods*). (*D* and *E*) Fine-sand (63–150 µm) contents and $\overline{SS}$ as proxies for CHC/northern ACC strength. (*F*) Oxygen isotope record of the east Antarctic European Project for Ice Coring in Antarctica Dronning Maud Land Ice Core (EDML) ice core (36) [Antarctic ice core chronology (AICC) 2012 age scale]. Numbers mark Antarctic Isotope Maxima and the largest Antarctic warmings from A1 to A4. (*G*) Oxygen isotope record of the Greenland North Greenland Ice Core Project ice core (36) (Greenland Ice Core Chronology 2005 age scale). Vertical gray bars mark inferred millennial-scale DP throughflow peaks that correspond with millennial-scale temperature maxima in Antarctica and Heinrich stadials (Hs) in Greenland. MIS, marine isotope stages; SMOW, standard mean ocean water.

that correspond to Heinrich stadials in Greenland (36). Enhanced DP throughflow during these warm periods is consistent with the previously suggested impact of the bipolar seesaw mechanism on the Southern Ocean (37–40), leading to, for example, surface water warming, enhanced upwelling, and a stronger ACC caused by southward-shifted westerlies. The last millennial-scale increase in flow speeds at ~17.5 ka coincides with Heinrich Stadial 1, the beginning of Southern Ocean upwelling and the end of the last ice age on a global scale (41). The reacceleration of sub-Antarctic DP transport matches the major deglacial warming in the sub-Antarctic Southeast Pacific and South Atlantic (42) (Fig. 4), suggesting a close coupling of DP throughflow to the initiation of Southern Hemisphere warming. Similar to the glacial–interglacial pattern,

our inferred millennial-scale changes in DP throughflow are paralleled by SST changes in proxy records from the Southeast Pacific (Ocean Drilling Program Site 1233) (20, 40) extending north to the cold tongue in the eastern tropical Pacific (43) (Fig. 3). These data imply that substantial changes in the oceanographic dynamics of the South Pacific Gyre are related to the northward deflection of ACC waters at millennial timescales.

Conclusions

Our study points to important changes of the cold water route in the global meridional overturning circulation on both glacial–interglacial and millennial timescales through sub-Antarctic DP transport, which generally weakens (increases) during cold (warm) climates. The glacial reduction of the cold water route occurred in concert with the well-documented decrease of the warm water route [Agulhas leakage (2)]. We, thus, propose that both of these oceanographic corridors are critical for the South Atlantic contribution to glacial meridional overturning circulation strength changes.

Most oceanographic observations and models identify that variations in the position and strength of the southern westerly wind belt (SWW) impact changes in the strength of the ACC and DP throughflow (44). This conceptual picture is consistent with our reconstructed glacial reduction of sub-Antarctic DP throughflow being linked to a northward shift of the SWW as supported by the majority of the proxy-based SWW reconstructions (45). In particular, the reconstructions from southern South America indicate a substantial decrease of the westerly winds over their present core zone in the vicinity of the northern DP during colder intervals (46). At the same time, stronger westerly winds extended northward as indicated by a variety of proxy records from the winter rain zone of Chile (45, 47) and are in line with our inferred strengthening of the South Pacific Gyre. In contrast to the proxy records pointing to a critical role of the SWW for DP throughflow and the global meridional overturning circulation during the past 65,000 y, current coupled ocean–atmosphere models do not show a coherent change in the position and strength of the SWW and the ACC during the LGM (48, 49). Hence, glacial ACC transport decreases might also be regulated by additional factors, such as Southern Ocean sea ice extent, that change the effective wind stress acting on the ocean surface (13).

Although still hypothetical, important paleoceanographic changes in the sub-Antarctic Southern Ocean are likely related to changes in the SWW. If applicable to modern timescales, the strengthening and poleward shift of the SWW seen in the Coupled Model Intercomparison Project Phase 5 (7) might lead to a future increase in sub-Antarctic DP transport, strengthening of the ACC, and enhanced interbasin exchange. However, recent instrumental volume transport time series across the DP have not yet revealed any significant increase in response to strengthened westerly winds (6). Thus, the response of the ACC to future climate changes remains a major challenge to be addressed.

Methods

We updated the published age models for cores MD07-3128 (19) and MR0806-PC09 (21), which are primarily based on radiocarbon dating. A detailed grain size analysis of the silt fraction (2–63 μm) and the fine-sand fraction (63–150 μm) was performed by measurements with a Micromeritics SediGraph 5100 (Fig. S3), a Coulter Counter, and a Beckman Coulter Laser Diffraction Particle Size Analyzer. The glacial reduction of DP throughflow was calculated from the mean $\overline{SS}$ values for the Holocene (0–11.5 ka) and the LGM sensu lato (18–28 ka). Geochemical data from core MD07-3128 were derived from discrete atomic absorption spectrophotometry measurements on discrete samples and high-resolution down-core scanning using an AVAATECH Profiling X-Ray Fluorescence Core Scanner.

ACKNOWLEDGMENTS. We thank the captain, crew, and scientific party of The International Marine Past Global Change Study *R/V Marion Dufresne* cruise MD159/PACHIDERME. We also thank V. Benz, C. Kissel, G. Knorr, G. Kuhn, N. McCave, and C. Purcell for discussions. We thank two anonymous reviewers for constructive comments. R. Ahi, R. Fröhlking, and S. Wiebe provided technical support at Alfred-Wegener-Institut (AWI). Financial support for this work was through the AWI Helmholtz-Zentrum für Polar- und Meeresforschung; the Center for Marine Environmental Sciences; Deutsche Forschungsgemeinschaft Grants LA 1273/3-2, LA1273/5-1, and KI-456/9-1; and the Helmholtz Network Regional Climate Change. C.B.L. received a 2014 fellowship from the Hanse-Wissenschaftskolleg. I.R.H. received funding from European Commission 7th Framework Marie Curie People Programme Initial Training Network GATEWAYS Grant 238512.

1. Marshall J, Speer K (2012) Closure of the meridional overturning circulation through Southern Ocean upwelling. *Nat Geosci* 5(3):171–180.
2. Beal LM, De Ruijter WPM, Biastoch A, Zahn R; SCOR/WCRP/IAPSO Working Group 136 (2011) On the role of the Agulhas system in ocean circulation and climate. *Nature* 472(7344):429–436.
3. Gordon AL (1986) Interocean exchange of thermocline water. *J Geophys Res* 91(C4): 5037–5046.
4. Cunningham SA, Alderson SG, King BA, Brandon MA (2003) Transport and variability of the Antarctic Circumpolar Current in Drake Passage. *J Geophys Res Oceans* 108(C5): 8084.
5. Meredith MP, et al. (2011) Sustained monitoring of the Southern Ocean at Drake Passage: Past achievements and future priorities. *Rev Geophys* 49:RG4005.
6. Koenig Z, Provost C, Ferrari R, Sennéchael N, Rio M-H (2014) Volume transport of the Antarctic Circumpolar Current: Production and validation of a 20 year long time series obtained from in situ and satellite observations. *J Geophys Res Oceans* 119(8): 5407–5433.
7. Meijers AJS (2014) The Southern Ocean in the Coupled Model Intercomparison Project phase 5. Philos *Trans* R Soc *Lond* A 372(2019):20130296.
8. Orsi AH, Whitworth T, Nowlin WD (1995) On the meridional extent and fronts of the Antarctic Circumpolar Current. *Deep Sea Res Part 1 Oceanogr Res Pap* 42(5):641–673.
9. Renault A, Provost C, Sennéchael N, Barré N, Kartavtseff A (2011) Two full-depth velocity sections in the Drake Passage in 2006—Transport estimates. *Deep Sea Res Part 2 Top Stud Oceanogr* 58(25-26):2572–2591.
10. Sokolov S, Rintoul SR (2009) Circumpolar structure and distribution of the Antarctic Circumpolar Current fronts: 1. Mean circumpolar paths. *J Geophys Res Oceans* 114: C11018.
11. Comiso JC (2003) Large-scale characteristics and variability of the global sea-ice cover. *Sea Ice: An Introduction to Its Physics, Chemistry, Biology and Geology*, eds Thomas DN, Diekmann GS (Blackwell, Oxford), pp 112–142.
12. Knorr G, Lohmann G (2003) Southern Ocean origin for the resumption of Atlantic thermohaline circulation during deglaciation. *Nature* 424(6948):532–536.
13. McCave IN, Crowhurst SJ, Kuhn G, Hillenbrand C-D, Meredith MP (2014) Minimal change in Antarctic Circumpolar Current flow speed between the last glacial and Holocene. *Nat Geosci* 11(7):113–116.
14. Mazaud A, Michel E, Dewilde F, Turon JL (2010) Variations of the Antarctic Circumpolar Current intensity during the past 500 ka. *Geochemistry, Geophysics, Geosystems* 11:Q08007.
15. Hall IR, McCave IN, Shackleton NJ, Weedon GP, Harris SE (2001) Intensified deep Pacific inflow and ventilation in Pleistocene glacial times. *Nature* 412(6849):809–812.
16. Weaver PPE, Carter L, Neil HL (1998) Response of surface water masses and circulation to late Quaternary climate change east of New Zealand. *Paleoceanography* 13(1): 70–83.
17. Well R, Roether W (2003) Neon distribution in South Atlantic and South Pacific waters. *Deep Sea Res Part 1 Oceanogr Res Pap* 50(6):721–735.
18. Chaigneau A, Pizarro O (2005) Surface circulation and fronts of the South Pacific Ocean, east of 120 degrees W. *Geophys Res Lett* 32(8):L08605.
19. Caniupán M, et al. (2011) Millennial-scale sea surface temperature and Patagonian Ice Sheet changes off southernmost Chile (53°S) over the past similar to 60 kyr. *Paleoceanography* 26:PA3221.
20. Kaiser J, Lamy F (2010) Links between Patagonian Ice Sheet fluctuations and Antarctic dust variability during the last glacial period (MIS 4-2). *Quat Sci Rev* 29(11-12):1464–1471.
21. Shiroya K, et al. (2013) Melting history of the Patagonian Ice Sheet during Termination I inferred from marine sediments. *Geochem J* 47(2):107–117.
22. McCave IN, Manighetti B, Robinson SG (1995) Sortable silt and fine sediment size composition slicing—parameters for paleocurrent speed and paleoceanography. *Paleoceanography* 10(3):593–610.
23. Boisvert WE (1969) Major currents off the west coasts of North and South America technical report. Technical Report (Naval Oceanographic Office, Washington, DC), p 34.
24. Firing YL, Chereskin TK, Mazloff MR (2011) Vertical structure and transport of the Antarctic Circumpolar Current in Drake Passage from direct velocity observations. *J Geophys Res Oceans* 116:C08015.
25. McCave IN, Hall IR, Bianchi GG (2006) Laser vs. settling velocity differences in silt grainsize measurements: Estimation of palaeocurrent vigour. *Sedimentology* 53(4): 919–928.
26. Thornalley DJR, et al. (2013) Long-term variations in Iceland-Scotland overflow strength during the Holocene. *Clim Past* 9(5):2073–2084.
27. Chen J, et al. (2006) Zr/Rb ratio in the Chinese loess sequences and its implication for changes in the East Asian winter monsoon strength. *Geochim Cosmochim Acta* 70(6): 1471–1482.

28. Ho SL, et al. (2012) Sea surface temperature variability in the Pacific sector of the Southern Ocean over the past 700 kyr. *Paleoceanography* 27:PA4202.
29. Nelson CS, Hendy IL, Neil HL, Hendy CH, Weaver PPE (2000) Last glacial jetting of cold waters through the Subtropical Convergence zone in the Southwest Pacific off eastern New Zealand, and some geological implications. *Palaeogeogr Palaeocl* 156(1-2): 103–121.
30. Ferrari R, et al. (2014) Heat fluxes across the Antarctic Circumpolar Current in Drake Passage: Mean flow and eddy contributions. *J Geophys Res Oceans* 119(9):6381–6402.
31. Bostock HC, Sutton PJ, Williams MJM, Opdyke BN (2013) Reviewing the circulation and mixing of Antarctic Intermediate Water in the South Pacific using evidence from geochemical tracers and Argo float trajectories. *Deep Sea Res Part 1 Oceanogr Res Pap* 73:84–98.
32. Martinez-Mendez G, et al. (2013) Changes in the advection of Antarctic Intermediate Water to the northern Chilean coast during the last 970 kyr. *Paleoceanography* 28(4): 607–618.
33. Muratli JM, Chase Z, Mix AC, McManus J (2010) Increased glacial-age ventilation of the Chilean margin by Antarctic Intermediate Water. *Nat Geosci* 3(1):23–26.
34. Makou MC, Oppo DW, Curry WB (2010) South Atlantic intermediate water mass geometry for the last glacial maximum from foraminiferal Cd/Ca. *Paleoceanography* 25(4):PA004101.
35. Liu ZY, et al. (2002) Tropical cooling at the last glacial maximum and extratropical ocean ventilation. *Geophys Res Lett* 29(10):1409.
36. EPICA Community Members (2006) One-to-one coupling of glacial climate variability in Greenland and Antarctica. *Nature* 444(7116):195–198.
37. Anderson RF, et al. (2009) Wind-driven upwelling in the Southern Ocean and the deglacial rise in atmospheric CO2. *Science* 323(5920):1443–1448.
38. Barrows TT, Juggins S, De Deckker P, Calvo E, Pelejero C (2007) Long-term sea surface temperature and climate change in the Australian-New Zealand region. *Paleoceanography* 22(2):PA002215.
39. Lamy F, et al. (2007) Modulation of the bipolar seesaw in the southeast Pacific during Termination 1. *Earth Planet Sci Lett* 259(3-4):400–413.
40. Lamy F, et al. (2004) Antarctic timing of surface water changes off Chile and Patagonian ice sheet response. *Science* 304(5679):1959–1962.
41. Denton GH, et al. (2010) The last glacial termination. *Science* 328(5986):1652–1656.
42. Barker S, Diz P (2014) Timing of the descent into the last Ice Age determined by the bipolar seesaw. *Paleoceanography* 29(6):PA002623.
43. Lea DW, et al. (2006) Paleoclimate history of Galápagos surface waters over the last 135,000 yr. *Quat Sci Rev* 25(11-12):1152–1167.
44. Völker C, Köhler P (2013) Responses of ocean circulation and carbon cycle to changes in the position of the Southern Hemisphere westerlies at Last Glacial Maximum. *Paleoceanography* 28(4):726–739.
45. Kohfeld KE, et al. (2013) Southern Hemisphere westerly wind changes during the Last Glacial Maximum: Paleo-data synthesis. *Quat Sci Rev* 68:76–95.
46. Lamy F, et al. (2010) Holocene changes in the position and intensity of the southern westerly wind belt. *Nat Geosci* 3:695–699.
47. Latorre C, et al. (2007) Late Quaternary environments and paleoclimate. The Geology of Chile, ed Gibbons WM (London Geological Society Press, London), pp 390–328.
48. Rojas M, et al. (2009) The Southern Westerlies during the last glacial maximum in PMIP2 simulations. *Clim Dyn* 32(4):525–548.
49. Sime LC, et al. (2013) Southern Hemisphere westerly wind changes during the Last Glacial Maximum: Model-data comparison. *Quat Sci Rev* 64:104–120.
50. Caniupán AM (2011) Paleoenvironmental history of the Chilean fjord region and the adjacent Southeast Pacific over the last 60 kyr BP: A multiproxy analysis on high resolution sediment cores. PhD thesis (Bremen University, Bremen, Germany).
51. Reimer PJ, et al. (2013) Intcal13 and Marine13 radiocarbon age calibration curves 0-50,000 years cal bp. *Radiocarbon* 55(4):1869–1887.
52. Siani G, et al. (2013) Carbon isotope records reveal precise timing of enhanced Southern Ocean upwelling during the last deglaciation. *Nat Commun* 4:2758.
53. Bazin L, et al. (2013) An optimized multi-proxy, multi-site Antarctic ice and gas orbital chronology (AICC2012): 120-800 ka. *Clim Past* 9(4):1715–1731.
54. Veres D, et al. (2013) The Antarctic ice core chronology (AICC2012): An optimized multi-parameter and multi-site dating approach for the last 120 thousand years. *Clim Past* 9(4):1733–1748.
55. Müller G (1967) *Methods in Sedimentary Petrology* (Schweizerbart'sche Velagsbuchhandlung, Stuttgart).
56. Bianchi GG, Hall IR, McCave IN, Joseph L (1999) Measurement of the sortable silt current speed proxy using the Sedigraph 5100 and Coulter Multisizer IIe: Precision and accuracy. *Sedimentology* 46(6):1001–1014.
57. McCave IN, Hall IR (2006) Size sorting in marine muds: Processes, pitfalls, and prospects for paleoflow-speed proxies. *Geochem Geophys Geosy* 7:Q10N05.
58. Prahl FG, Rontani J-F, Zabeti N, Walinsky SE, Sparrow MA (2010) Systematic pattern in UK'37: Temperature residuals for surface sediments from high latitude and other oceanographic settings. *Geochim Cosmochim Acta* 74(1):131–143.
59. Luz B (1977) Late Pleistocene paleoclimates of the South Pacfic based on statistical analysis of planktonic foraminifers. *Palaeogeogr Palaeocl* 22:61–78.
60. Mashiotta TA, Lea DW, Spero HJ (1999) Glacial-interglacial changes in Subantarctic sea surface temperature and delta O-18-water using foraminiferal Mg. *Earth Planet Sci Lett* 170(4):417–432.
61. Calvo E, Pelejero C, Herguera JC, Palanques A, Grimalt JO (2001) Insolation dependence of the southeastern Subtropical Pacific sea surface temperature over the last 400 kyrs. *Geophys Res Lett* 28(12):2481–2484.
62. Kaiser J, Schefuss E, Lamy F, Mohtadi M, Hebbeln D (2008) Glacial to Holocene changes in sea surface temperature and coastal vegetation in north central Chile: High versus low latitude forcing. *Quat Sci Rev* 27(21-22):2064–2075.
63. Kim JH, Schneider RR, Hebbeln D, Muller PJ, Wefer G (2002) Last deglacial sea-surface temperature evolution in the Southeast Pacific compared to climate changes on the South American continent. *Quat Sci Rev* 21(18-19):2085–2097.
64. Romero OE, Kim JH, Hebbeln D (2006) Paleoproductivity evolution off central Chile from the Last Glacial Maximum to the Early Holocene. *Quat Res* 65(3):519–525.
65. Pena LD, Cacho I, Ferretti P, Hall MA (2008) El Nino-Southern Oscillation-like variability during glacial terminations and interlatitudinal teleconnections. *Paleoceanography* 23(3):PA003101.
66. Rincon-Martinez D, et al. (2010) More humid interglacials in Ecuador during the past 500 kyr linked to latitudinal shifts of the equatorial front and the Intertropical Convergence Zone in the eastern tropical Pacific. *Paleoceanography* 25:PA2210.

Supporting Information

Lamy et al. 10.1073/pnas.1509203112

SI Methods

Sediment Cores. Sediment core MD07-3128 was retrieved from the southern Chilean continental slope ~30 nm off the Pacific entrance to the Strait of Magellan (52°39.57′ S, 75°33.97′ W; 1,032-m water depth). The site is located below the CHC, a branch of the ACC that continues toward the DP, where it joins the main sub-Antarctic ACC (Fig. 1 and Fig. S1). The sediment sequence consists of an upper unit of olive to yellow foraminifera ooze comprising the upper ~0.5 m of the core. This unit, representing the Holocene, is underlain by sand-bearing clayey silt to silty clay (the main lithology down to the base of the core representing the last glacial). This unit reveals meter-scale variations in color between gray and grayish olive, with occasional visually observed drop stones. These color changes largely parallel the variations in grain size and geochemistry shown in this paper. $CaCO_3$ contents are between ~30 and 55 wt % in the Holocene and between ~1 and 12 wt % for the glacial part. Biogenic silica and organic matter contents range from 1 to 4 wt % and from 0.3 to 0.8 wt %, respectively, throughout the core (50).

Sediment core MR0806-PC09 was recovered from the southernmost Argentinean continental slope to the east of Cape Horn (55°42.58′ S, 66°08.06′ W; 684-m water depth) within the northern sector of the DP (Fig. S1). The upper surface unit (0.11 m) consists of fine to medium foraminifer sand. Below, the sediments are mostly dark gray clayey silt with lenses and layers of fine sand; they are bioturbated, and ice-rafted debris is observed down to 7.8 m. A detailed lithological description is given by Shiroya et al. (21). $CaCO_3$ contents range from 25 to 37 wt % in the Holocene and from 1 to 15 wt % for the glacial. Biogenic silica and organic carbon contents are 2–4 and 0.1–0.4 wt %, respectively, throughout the core.

Age Models. We updated the published age models for cores MD07-3128 (19) and MR0806-PC09 (21) by using the most recent calendar age conversion curve INTCAL13 and software Calib 7.0 (51). Moreover, we considered the recent reservoir age estimates for the Holocene and the last deglaciation from core MD07-3088 located northward (46° S) at the Chilean continental margin (52). We used the oldest reservoir age given by Siani et al. (52) as an estimate for glacial reservoir ages at our core location. For core MD07-3128, we kept the age control point represented by the Laschamp magnetic field excursion at ~41,250 y ago (19). The preradiocarbon part of the age model of core MD07-3128 is based on graphical tuning of the alkenone SST record to that of the composite sequence at Ocean Drilling Program Site 1233 (20) (Fig. S2). Age control points are given in Table S1.

We also updated the age model of the Ocean Drilling Program Site 1233 sediment record. As for cores MD07-3128 and MR0806-PC09, we used the most recent calendar age calibration curves and the reservoir age estimates by Siani et al. (52), except for the Holocene. During this time interval, we assumed the global value of ~400 y, consistent with the occurrence of an early Holocene ash layer at Site 1233 that has been dated on land (40). We updated the preradiocarbon part of the Site 1233 age model, which was originally based on tuning of the SST record to the oxygen isotope record of the Byrd ice core (20, 40), by graphical tuning to the European Project for Ice Coring in Antarctica Dronning Maud Land Ice Core (EDML) record on the most recent Antarctic ice core chronology (AICC) 2012 (53, 54). Age control points are given in Table S1.

Grain Size Determinations. Grain size data were obtained from cores MD07-3128 and MR0806-PC09 (Figs. S3 and S4). For core MD07-3128, samples for grain size measurements were taken at a spacing of 12 cm, with an average temporal resolution of ~2,800 y for the upper part of the core corresponding to the Holocene and ~200–250 y for the glacial section. To separate the terrigenous sediment fraction, we used 35% (vol/vol) H_2O_2 to remove organic matter and for disaggregation and 10% (vol/vol) acetic acid to dissolve carbonate. Because biogenic silica contents are low (1 to 4 wt %), we did not dissolve opal. The separation of the 63- to 150-μm fine-sand fraction was achieved by wet sieving, whereas the silt (2–63 μm) and clay fractions (<2 μm) were split by Stokes' law settling using Atterberg tubes (55). To separate the latter two size fractions almost completely, a 9- to 12-times repetition of the settling procedure was necessary. Coagulation of clay size particles was avoided by using a 0.1% sodium polyphosphate solution.

A detailed grain size analysis of the silt fraction (2–63 μm) and the fine-sand fraction (63–150 μm) was performed by measurements with a Micromeritics SediGraph 5100 (Fig. S3) at the Alfred Wegener Institute. The SediGraph also detects the remaining >150-μm sand and clay particles in the silt fraction, which have not been removed by Atterberg and sieving methods. The SediGraph analysis provides a high-resolution grain size distribution in steps of 0.1 ϕ and is based on the X-ray scanning of a settling suspension assuming Stokes' law settling. $\overline{SS}$ is the mean grain size of the SS fraction (10–63 μm) as defined by McCave et al. (22). The instrument precision of the SediGraph 5100 for pure standard analysis is from ±0.3% to ±1.9% (56). Marine sediments with >5% SS yielded an analytical precision for $\overline{SS}$ measurements and the weight percentages of SS of ±2% and ±9%, respectively (56).

The Holocene section contains only very small amounts of terrigenous components, because it is primarily composed of biogenic carbonate. Therefore, we could not reliably measure terrigenous silt and fine sand with the SediGraph for this interval, because the amount was too small. We, thus, used a polynomial regression between strongly covarying $\overline{SS}$ and fine-sand contents for the glacial section (Fig. S3) to derive Holocene $\overline{SS}$ estimates. Typical Holocene values were estimated in the range of ~40 μm based on fine-sand contents of ~55 wt %.

The SediGraph is generally considered as the best suited device for measuring grain size as a proxy for current intensity, because it uses the settling velocity principle measuring dynamical grain sizes closely related to transport and depositional processes (57). We compared our data with measurements with a Coulter Counter at Cardiff University on selected samples, and they showed very similar results (Fig. S6). The Coulter Counter measures the volume equivalent spherical diameter through electrical conductivity. The similar results obtained by these different devices support the robustness of our grain size measurement.

For core MR0806-PC09, samples for grain size measurements were taken at a spacing of 2–5 cm, with an average temporal resolution of ~1,000–4,000 y for the upper part of the core corresponding to the Holocene and ~100–300 y for the glacial section. Grain size measurements were performed with Beckman Coulter Laser Diffraction Particle Size Analyzer Type LS 13320 at the MARUM Center. The laser itself is equipped with an Aquous Liquid Module and an Auto Prep Station, and it determines particle grain sizes from 0.04 to 2,000 μm grouped into 116 size classes. Moreover, the laser uses degassed water to avoid bubbles during the measurements. Instrumental precision based

on repeated sample diffraction is ≤3%. Before grain size analyses, we isolated the terrigenous fraction. Organic material was removed with ~10 mL H_2O_2 (35%) and calcium carbonate with HCl (10%). Finally, the samples were boiled with 300 mg sodium pyrophosphate ($Na_4P_2O_7$*10H_2O) to ensure disaggregation of all particles. Because biogenic silica contents are low (2–4 wt %), we did not dissolve opal.

Glacial DP Throughflow Estimate. We calculated the glacial DP flow speed by combining the $\overline{SS}$ record from CHC/northern ACC sites MD07-3128 and MR0806-PC09 with published $\overline{SS}$ records from the southern Polar Frontal Zone and Antarctic Zone of the ACC in the Scotia Sea (13). To compare the individual reconstructed current speed records with modern DP current velocity and volume transport data, we projected each core onto the oceanographic Jason Track 104 crossing the DP downstream of the Shackleton Fracture Zone (Fig. S1*C*) beginning at the upper South American continental slope close to our core site MR0806-PC09. Core MD07-3128, likewise, projects on the northern end of the section, because it is located below the CHC that contributes to sub-Antarctic DP throughflow (Fig. S1). The Scotia Sea cores were projected onto track 104 using the Scotia Sea projection line by McCave et al. (13) and the relative distances between the major climatological oceanic fronts (Table S2). The glacial reduction of DP throughflow was calculated from the mean $\overline{SS}$ values for the Holocene (0–11.5 ka) and the LGM sensu lato (18–28 ka).

Geochemistry. Geochemical data from core MD07-3128 include major and minor element concentrations (Fig. S5), which were derived from discrete atomic absorption spectrophotometry measurements on the bulk sediment. Measurements were performed with a VARIAN SepctrAA220 at the University of Trier. Samples of 100 mg sediment were dried (105 °C) and fused completely in Pt skillets with 400 mg flux material (mixture of lithiumtetraborate, lithium carbonate, and lanthanium oxide). The produced glass beads were dissolved in 40 mL HCl (0.5 N). Liquids of samples and international standards (MRG-1, SY-2, and JG-2) were measured by the atomic absorption spectrophotometry. Determined major elements plus loss of ignition (1,050 °C) and independently detected contents of CO_2 and SO_2 resulted in sums of 99–101 wt %. Zr and Rb concentrations were measured at 1-cm down-core resolution using an AVAATECH Profiling X-Ray Fluorescence Core Scanner at the Alfred Wegener Institute.

SST. SST changes between the Holocene and the LGM in the Southeast Pacific have been compiled from published records (Fig. 3 and Table S3). These records include primarily alkenone-based SST reconstructions, except for two Mg/Ca-derived SST records from the eastern tropical Pacific and one from the East Pacific Rise. We also added published foraminifera transfer function-based SSTs from the East Pacific Rise.

Where possible, we calculated glacial cooling (Fig. 3 and Table S3) from the temperature difference between the mean Holocene (0–11.5 ka) and the LGM sensu stricto (19–23 ka) SST estimates. This method provides glacial cooling estimates based on proxy SSTs uninfluenced by potential offsets of the absolute proxy calibration to modern world ocean atlas SSTs. Note that the LGM SSTs based on foraminifera assemblage are winter estimates, whereas the alkenone SSTs, at least for the southern sector, most likely represent spring/summer temperatures (28, 58).

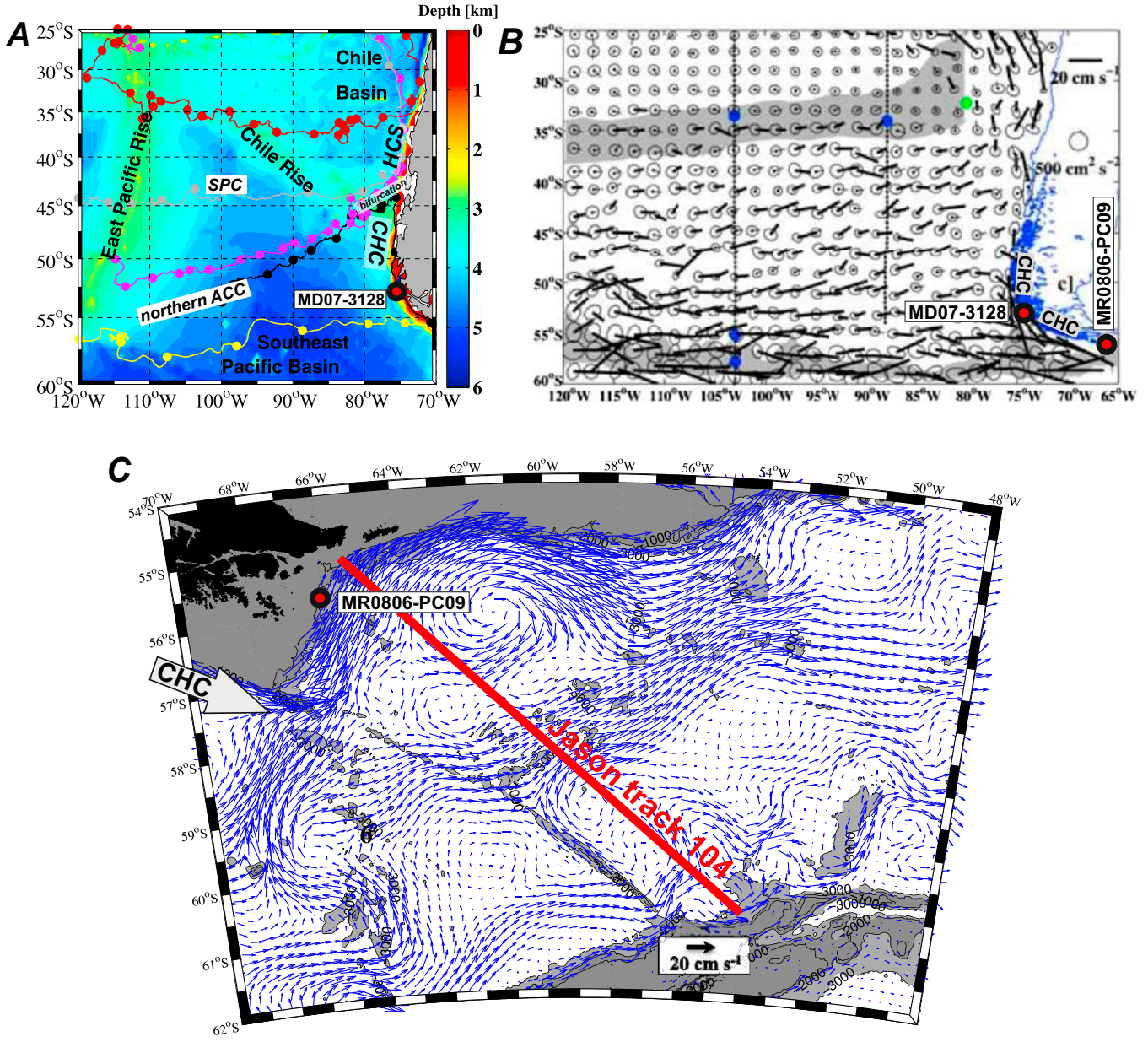

Fig. S1. Surface and intermediate ocean circulation in the Southeast Pacific. (*A*) Examples of surface buoy trajectories (each 30-d position is indicated by a circle) indicating northeast flow of northern ACC water after crossing the East Pacific Rise. Also shown is the bifurcation of surface waters close to the Chilean coast (at ~45° S), with northward flowing water in the Humboldt Current System (HCS) and strongly accelerated southward flow in the Cape Horn Current (CHC) toward the DP. West–east drifting buoys follow the South Pacific Current (SPC). (*B*) Surface velocities and velocity variance ellipses from drifter measurements (velocities >6 cm/s are bold). Note the high current velocities in the southern CHC in vicinity of our core MD07-3128 location. The drifter measurements are averaged to 2° × 2°-grid boxes, each of which contains more than five daily positions. (*C*) Mean velocity vectors at 500 m from model outputs (blue arrows) showing strong flow along the northern border of the DP, where core MR0806-PC09 is located. The red line indicates the location of Jason Track 104. Modified from refs. 18 and 30.

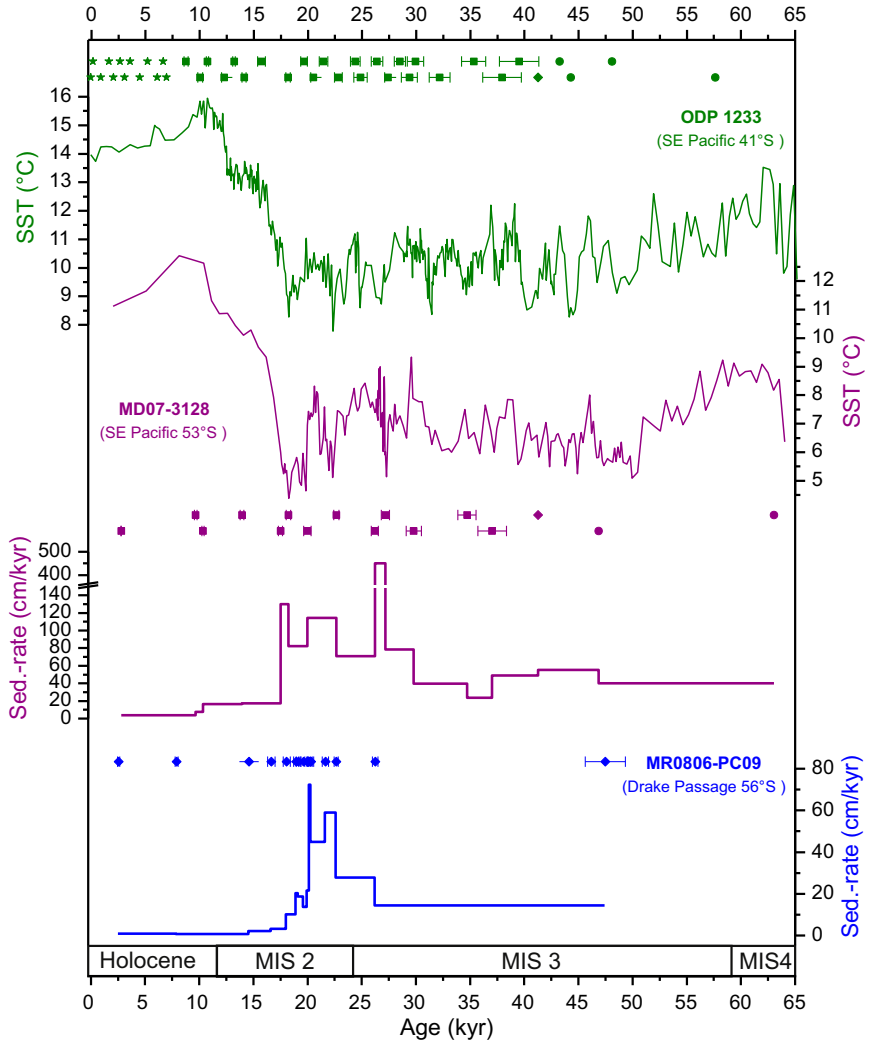

Fig. S2. Age models for cores MD07-3128 and MR0806-PC09. Age control is based on radiocarbon dates (■ with 2σ errors) [updated from the works by Caniupán et al. (19) and Shiroya et al. (21)]. Additionally, for core MD07-3128, we used the paleomagnetic Laschamp excursion (◆) and graphical tuning of the SST record to that of Ocean Drilling Program (ODP) Site 1233 in the Southeast (SE) Pacific. The age model of the sediment sequence at Site 1233 has been updated from ref. 20. Additional details are in *SI Methods*, *Age Models*. Linear sedimentation rates (sed.-rate) for cores MD07-3128 and MR0806-PC09 are shown in *Bottom*. MIS, marine isotope stage.

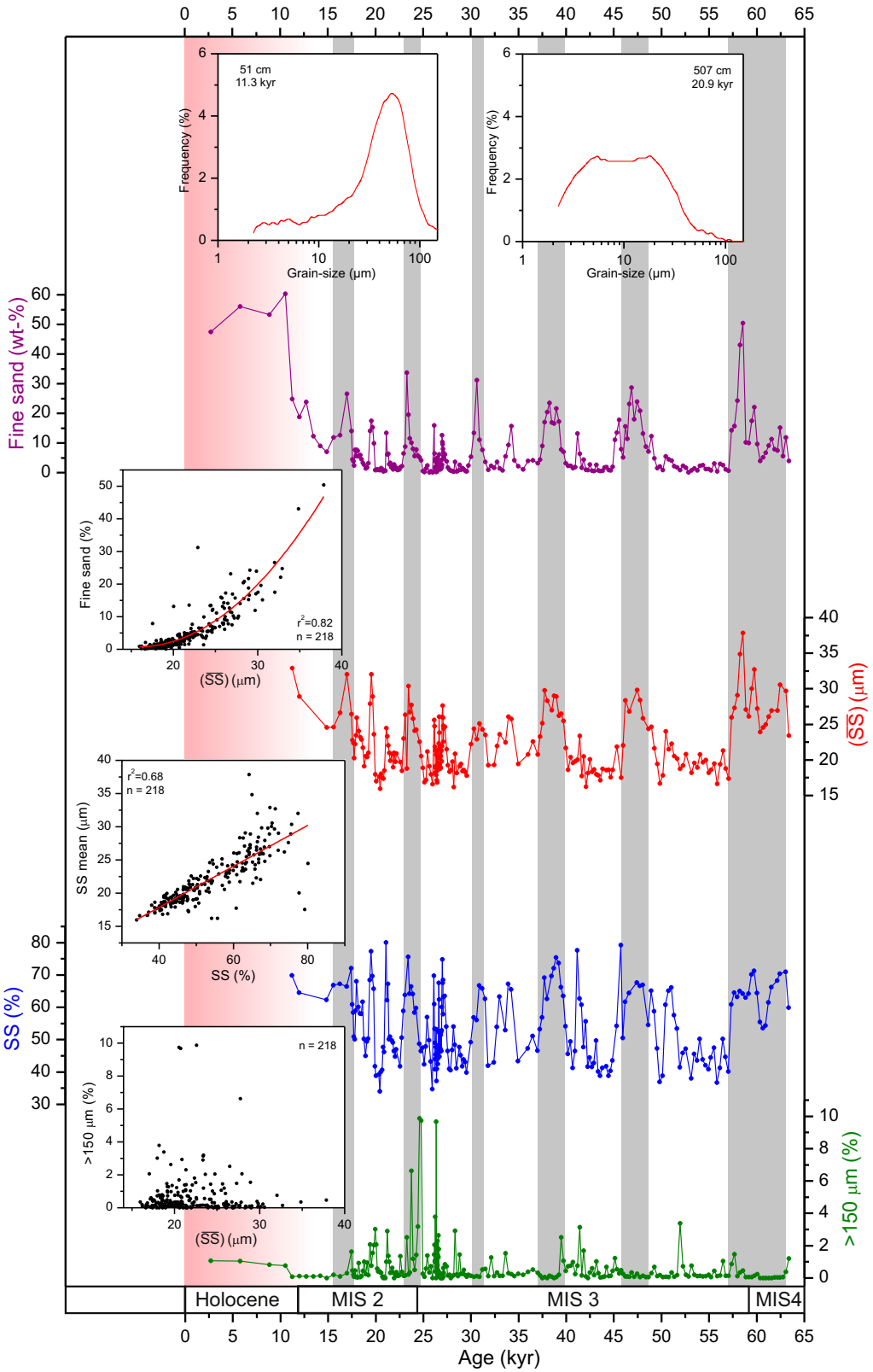

Fig. S3. Down-core grain size data from MD07-3128. Fine-sand content (purple), $\overline{SS}$ (red), SS percentage (blue), and >150-μm fraction [ice-rafted debris (IRD); green] (19). *Insets* in row 1 show contrasting fine-sand and silt grain size distributions from representative (*Left Inset*) early Holocene and (*Right Inset*) LGM samples. *Insets* in rows 2–4 show (*Inset* in row 2) polynomial regression between fine sand and $\overline{SS}$, (*Inset* in row 3) linear relation between $\overline{SS}$ and SS percentage, and (*Inset* in row 4) uncorrelated IRD with $\overline{SS}$. Vertical gray bars mark inferred millennial-scale DP throughflow maxima (like in Fig. 4). MIS, marine isotope stage.

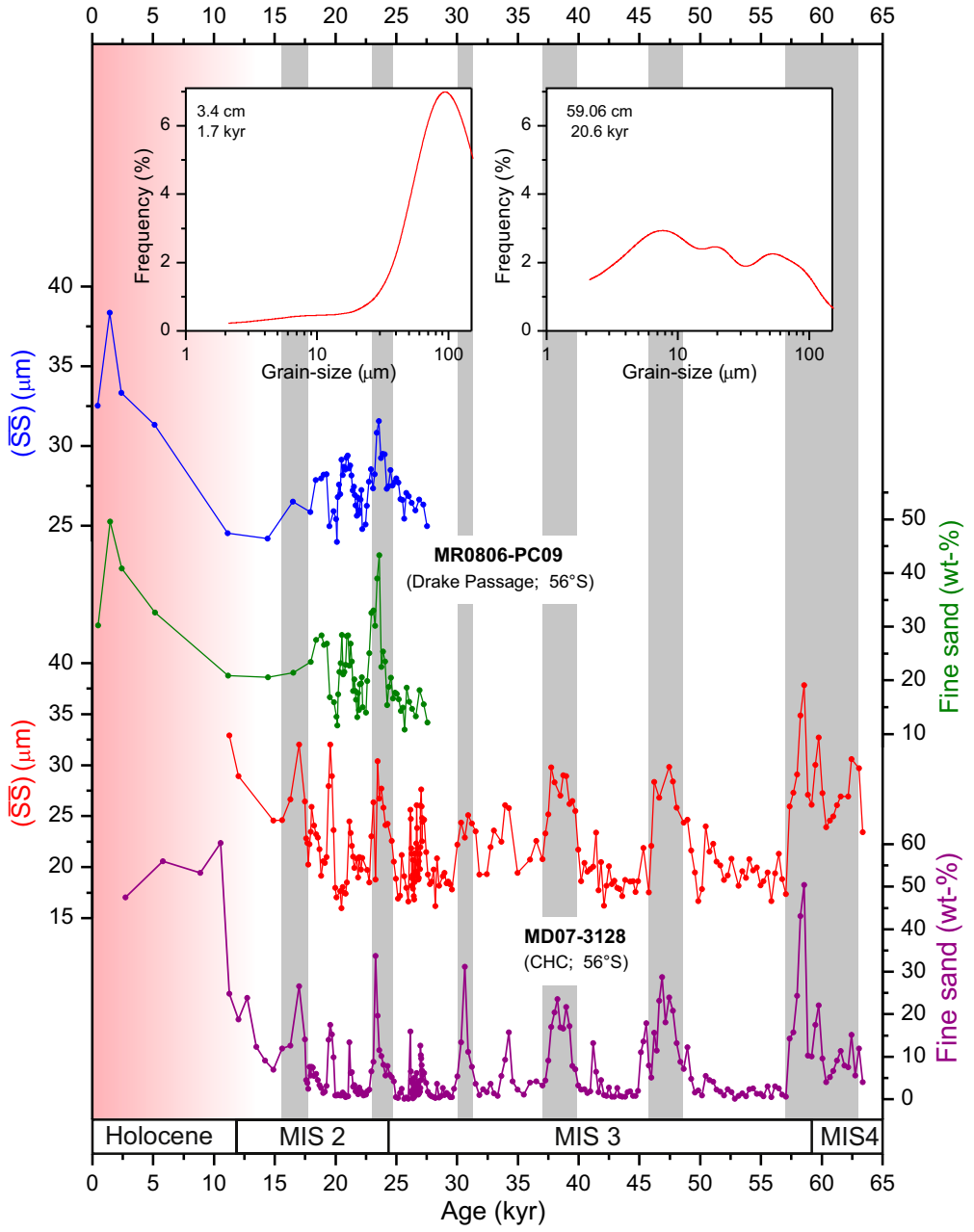

Fig. S4. Grain size data from cores MR0806-PC09 and MD07-3128. $\overline{SS}$ (blue) and fine-sand (green) down-core records from core MR0806-PC09. *Insets* show contrasting fine-sand and silt grain size distributions from representative (*Left Inset*) early Holocene and (*Right Inset*) LGM samples. Red and purple down-core records show $\overline{SS}$ and fine-sand contents of core MD07-3128, respectively. Vertical gray bars mark inferred millennial-scale DP throughflow maxima (like in Fig. 4). MIS, marine isotope stage.

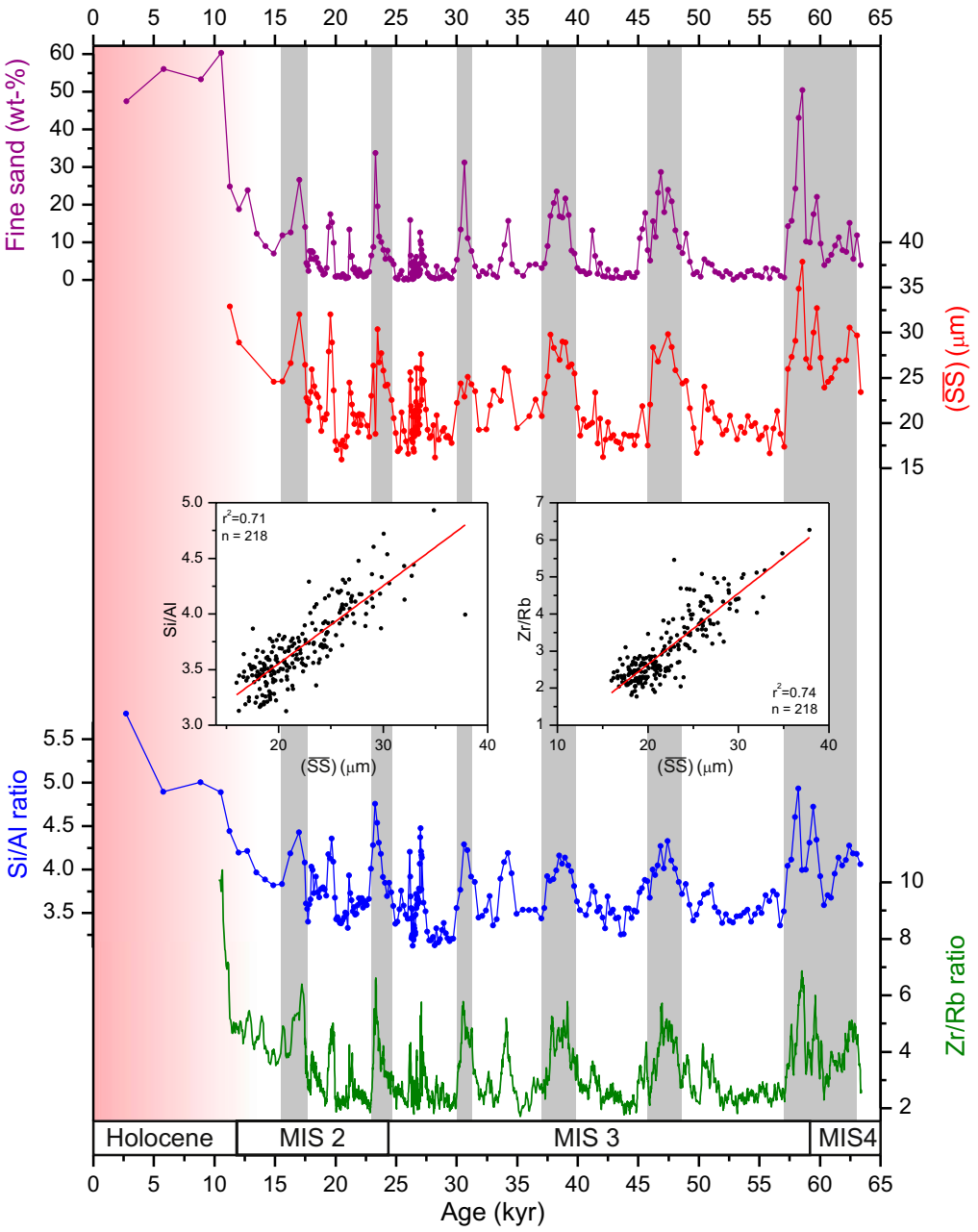

Fig. S5. Geochemistry data from core MD07-3128. Fine-sand contents (purple) and $\overline{SS}$ (red) compared with down-core records of Si/Al (blue) and Zr/Rb (green; five-point moving average) ratios. Because biogenic silica contents are very low (<4 wt %), Si contents reflect primarily changes in the siliciclastic fraction. This assumption is consistent with covarying changes in both Si/Al and Zr/Rb ratios primarily reflecting grain size changes. Vertical gray bars mark inferred millennial-scale DP throughflow maxima (like in Fig. 4). MIS, marine isotope stage.

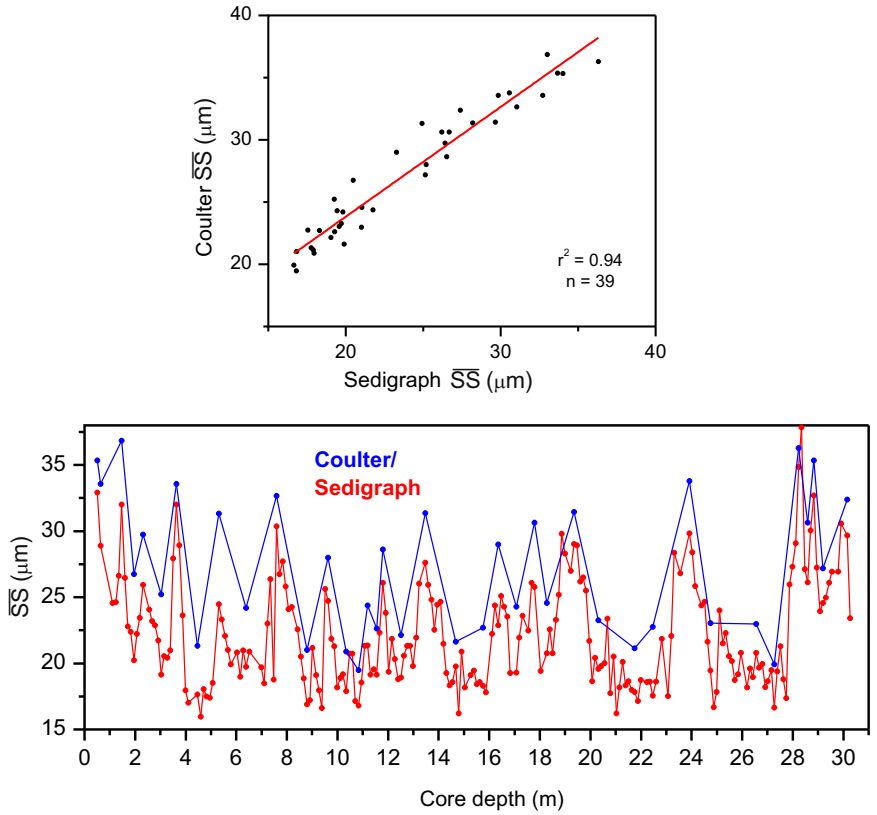

Fig. S6. Comparison between $\overline{SS}$ obtained from Sedigraph and Coulter Counter measurements in core MD07-3128. (*Upper*) The similar results obtained by these different devices support the robustness of our grain size measurement. (*Lower*) Absolute Coulter Counter $\overline{SS}$ values tend to be slightly higher, but amplitudes are generally consistent.

Table S1. Age control points for the construction of age models for cores MD07-3128 and MR0806-PC09 and the Ocean Drilling Program Site 1233 sediment record [update of the published age models (19–21)]

Core depth (m/mcd)	^{14}C raw age (ka)	±Error (ky)	Reservoir age (ky)	Calibrated age (ka)	±Error (ky)	Dating method
MD07-3128						
0.03	3.41	0.025	0.80	2.75	0.02	INTCAL13
0.3	9.49	0.045	0.81	9.63	0.12	INTCAL13
0.35	9.95	0.045	0.81	10.29	0.10	INTCAL13
0.94	13.04	0.06	0.98	13.91	0.16	INTCAL13
1.55	15.46	0.07	1.13	17.46	0.24	INTCAL13
2.5	16.10	0.07	1.13	18.19	0.21	INTCAL13
3.93	17.33	0.13	0.81	19.93	0.34	INTCAL13
7	19.56	0.1	0.81	22.62	0.24	INTCAL13
9.52	22.76	0.15	0.81	26.17	0.33	INTCAL13
13.96	23.61	0.15	0.81	27.16	0.38	INTCAL13
16.01	26.40	0.24	0.81	29.76	0.68	INTCAL13
17.96	31.54	0.465	0.81	34.69	0.85	INTCAL13
18.51	33.66	0.54	0.81	37.02	1.33	INTCAL13
20.58				41.25		Laschamp
23.67				46.85		Tuning
30.16				63.06		Tuning
MR0806-PC09						
0.06	3.21	0.05	0.80	2.45	0.10	INTCAL13
0.10	7.76	0.08	0.81	7.80	0.14	INTCAL13
0.15	13.6	0.08	1.23	14.49	0.40	INTCAL13
0.19	15.0	0.11	1.32	16.55	0.36	INTCAL13
0.24	15.65	0.13	0.89	17.97	0.32	INTCAL13
0.33	16.4	0.11	0.81	18.85	0.24	INTCAL13
0.37	16.6	0.09	0.81	19.07	0.23	INTCAL13
0.46	17.0	0.12	0.81	19.55	0.34	INTCAL13
0.51	17.3	0.09	0.81	19.88	0.26	INTCAL13
0.55	17.45	0.08	0.81	20.09	0.24	INTCAL13
0.64	17.55	0.08	0.81	20.21	0.24	INTCAL13
1.24	18.6	0.09	0.81	21.55	0.29	INTCAL13
1.82	19.45	0.09	0.81	22.54	0.20	INTCAL13
2.82	22.7	0.12	0.81	26.14	0.27	INTCAL13
5.89	44.8	0.87	0.81	47.40	1.84	INTCAL13
ODP 1233						
10.55	8.3	0.06	0.40	8.74	0.19	INTCAL13
12.94	9.34	0.08	0.40	10.04	0.23	INTCAL13
14.21	9.87	0.05	0.40	10.72	0.11	INTCAL13
17.01	10.8	0.07	0.40	12.27	0.25	INTCAL13
20.22	12.28	0.07	0.95	13.18	0.12	INTCAL13
21.39	13.18	0.06	0.98	14.10	0.19	INTCAL13
25.1	14.42	0.11	1.32	15.70	0.36	INTCAL13
27.97	15.75	0.07	0.81	18.16	0.21	INTCAL13
29.81	17.07	0.11	0.81	19.64	0.32	INTCAL13
31.47	17.81	0.09	0.81	20.51	0.27	INTCAL13
33.51	18.52	0.13	0.81	21.44	0.39	INTCAL13
36.56	19.74	0.14	0.81	22.80	0.36	INTCAL13
39.5	21.08	0.15	0.81	24.36	0.45	INTCAL13
41.17	21.44	0.24	0.81	24.85	0.62	INTCAL13
43.72	22.93	0.23	0.81	26.37	0.54	INTCAL13
45.53	23.88	0.17	0.81	27.38	0.30	INTCAL13
47.25	25.28	0.24	0.81	28.50	0.52	INTCAL13
49.11	26.1	0.29	0.81	29.37	0.74	INTCAL13
50.72	26.52	0.30	0.81	29.92	0.75	INTCAL13
55.02	29.03	0.39	0.81	32.16	0.95	INTCAL13
59.03	32.19	0.58	0.81	35.31	1.11	INTCAL13
62.5	34.48	0.75	0.81	37.92	1.78	INTCAL13
64.81	35.77	0.79	0.81	39.50	1.83	INTCAL13
67.8				41.25		Laschamp
73.54				43.23		Tuning
76.03				44.28		Tuning
82.60				48.09		Tuning

Table S1. Cont.

Core depth (m/mcd)	^{14}C raw age (ka)	±Error (ky)	Reservoir age (ky)	Calibrated age (ka)	±Error (ky)	Dating method
100.08				57.63		Tuning
129.10				70.59		Tuning
134.84				73.47		Tuning

mcd, meter composite depth; ODP, Ocean Drilling Program.

Table S2. Holocene and LGM (sensu lato; 18–28 ka) mean $\overline{SS}$ data across the DP, including data south of the SAF in the Scotia Sea (13) (Fig. 1)

Site	Holocene $\overline{SS}$ mean (μm)	$2\sigma/\sqrt{n}$	LGM $\overline{SS}$ mean (μm)	$2\sigma/\sqrt{n}$	LGM $\overline{SS}$ reduction (%)	Projected on Track 104	Location on the line by McCave et al. (13)
MD07-3128	38.3	2.537	21.4	0.692	−44	30	n/a
MR0806-PC09	33.9	2.683	27.3	0.383	−19	30	n/a
SAF	n/a	n/a	n/a	n/a	n/a	80	n/a
SSAF	n/a	n/a	n/a	n/a	n/a	280	15
BAS TPC063	21.37	0.604	19.78	0.62	−7	337	110
BAS TPC077	19.6	0.811	20.29	0.597	4	423	250
APF	n/a	n/a	n/a	n/a	n/a	465	330
PS2514-1	18.97	0.463	19.57	0.615	3	505	360
PS67/197–1	17.35	0.625	17.72	0.499	2	538	425
BAS TC290/PC078	16.11	0.334	16.86	0.283	5	590	480
PS67/205–2	18.06	0.561	16.2	0.261	−10	691	610
PS67/219–1	17.84	0.238	16.58	0.54	−7	715	680
SACCF	n/a	n/a	n/a	n/a	n/a	780	720
PS67/224–1	15.97	0.261	15.47	0.315	−3	806	735

Note that $2\sigma/\sqrt{n}$ is the SEM. The analytical error of up to ±3% has not been propagated. Approximate locations are based on refs. 8 and 10. APF, Antarctic PF; BAS, British Antarctic Survey; n/a, not applicable; SACCF, southern ACC front; SSAF, southern SAF.

Table S3. Summary of SST records shown in Fig. 3

Core	Latitude	Longitude	Holocene SST (°C)	LGM × SST (°C)	LGM − Holocene (°C)	SST method	Ref.
East Pacific Rise (central Pacific)							
E20-18	−44.55	248.67	9*	9.2†	0.2	Foraminifera	Luz (59)
DWBG-70	−48.48	246.72	6*	2.6†	−3.4	Foraminifera	Luz (59)
E25-10	−50.10	245.22	6*	1.1†	−4.9	Foraminifera	Luz (59)
E21-15	−52.02	239.98	5*	1.1†	−3.9	Foraminifera	Luz (59)
RC12-225	−53.67	236.90	4*	1.1†	−2.9	Foraminifera	Luz (59)
E11-1	−54.91	245.30	3*	0.7†	−2.3	Foraminifera	Luz (59)
E11-3	−56.90	244.76	2*	0.6†	−1.4	Foraminifera	Luz (59)
E11-2	−56.06	244.94	3*	0.6†	−2.4	Foraminifera	Luz (59)
E11-2	−56.06	244.94	4.7	2.8	−1.9	Mg/Ca	Mashiotta et al. (60)
Southeast Pacific							
TG7	−17.20	281.40	20.4	17.3	−3.1	Alkenones	Calvo et al. (61)
GeoB7139	−30.20	288.02	18.5	15	−3.5	Alkenones	Kaiser et al. (62)
GeoB3302	−33.22	287.91	17.4‡	12.7	−4.7	Alkenones	Kim et al. (63)
GeoB3359	−35.22	287.20	18	12.4	−5.6	Alkenones	Romero et al. (64)
ODP 1233	−41.00	285.55	14.9	9.9	−5.0	Alkenones	Kaiser and Lamy (20)
MD07-3128	−52.66	284.44	12.1	6.5	−5.6	Alkenones	Caniupán et al. (19)
PS75/034–1	−54.65	279.85	8.6	1.5	−7.1	Alkenones	Ho et al. (28)
East tropical Pacific							
TR163-22	0.52	267.60	24.4	22.4	−2.0	Mg/Ca	Lea et al. (43)
ODP 1240	0.02	273.54	25.6	23.1	−2.5	Mg/Ca	Pena et al. (65)
ODP 1239	−0.67	277.92	24.9	23.4	−1.5	Alkenones	Rincon-Martinez et al. (66)

LGM sensu stricto (19–23 ka). ODP, Ocean Drilling Program.
*Modern winter SSTs (60).
†LGM winter SSTs (60).
‡Holocene values from neighboring core GIK17748.